Noname manuscript No.
(will be inserted by the editor)

A monolithic approach to fluid-composite structure interaction

Davide Forti · Martina Bukac · Annalisa Quaini · Suncica Canic · Simone Deparis

Received: date / Accepted: date

Abstract We study a nonlinear fluid-structure interaction (FSI) problem between an incompressible, viscous fluid and a composite elastic structure consisting of two layers: a thin layer (membrane) in direct contact with the fluid, and a thick layer (3D linearly elastic structure) sitting on top of the thin layer. The coupling between the fluid and structure, and the coupling between the two structures is achieved via the kinematic and dynamic coupling conditions modeling no-slip and balance of forces, respectively. The coupling is evaluated at the moving fluid-structure interface with mass, i.e., the thin structure. To solve this nonlinear moving-boundary problem in 3D, a monolithic, fully implicit method was developed, and combined with an Arbitrary Lagrangian-Eulerian (ALE) approach to deal with the motion of the fluid domain.

This class of problems and its generalizations are important in e.g., modeling FSI between blood flow and arterial walls, which are known to be composed of several different layers, each with different mechanical characteristics and thickness. By using this model we show how multi-layered structure of arterial walls influences the pressure wave propagation in arterial walls, and how the presence of atheroma and the presence of a vascular device called a stent, influence intramural strain distribution throughout different layers of the arterial

Davide Forti and Simone Deparis
CMCS - Chair of Modeling and Scientific Computing, MATHICSE - Mathematics Institute of Computational Science and Engineering, EPFL - École Polytechnique Fédérale de Lausanne, Station 8, Lausanne CH-1015, Switzerland
E-mail: davide.forti@epfl.ch; simone.deparis@epfl.ch

Martina Bukac
Department of Applied and Computational Mathematics and Statistics, University of Notre Dame, 158 Hurley Hall, Notre Dame, IN 46556, USA
E-mail: mbukac@nd.edu

Annalisa Quaini and Suncica Canic
Department of Mathematics, University of Houston, 4800 Calhoun Rd, Houston TX 77204, USA
E-mail: quaini@math.uh.edu; canic@math.uh.edu

wall. The detailed intramural strain distribution provided by this model can be used in conjunction with ultrasound B-mode scans as a predictive tool for an early detection of atherosclerosis [61].

1 Introduction

This work is motivated by a study of fluid-structure interaction (FSI) between blood flow and vascular tissue in normal and diseased states. Vascular tissue is a composite structure made of several different layers, each with different mechanical characteristics and thickness. So far there have been no realistic 3D FSI simulations that take into account the multi-layered structure of arterial walls. In this paper we present a monolithic computational model of FSI where the structure consists of two layers: a thin layer in direct contact with the fluid, and a thick layer sitting on top of the thin layer. The thin layer is modeled using the membrane model proposed in [25, 24], while the thick layer is modeled using the equations of 3D linear elasticity. The Navier-Stokes equations for an incompressible, viscous fluid are used to model the fluid flow. The fluid and structure are coupled via two conditions: the kinematic coupling condition describing continuity of velocities (no-slip), and the dynamic coupling condition describing the balance of contact forces. The coupling is evaluated at the deformed fluid-structure interface, which, in this problem, is the thin structure with mass. The coupling between the thin and thick structure is modeled via the kinematic and dynamic coupling conditions as well. The kinematic coupling condition describes continuity of displacement (glued structures) and the dynamic coupling condition describes the balance of contact forces, as before. Thus, across the thin fluid-structure interface with mass, the dynamic coupling condition states that the elastodynamics of the thin structure is driven by the jump in the normal stress coming from the fluid on one side, and the thick structure on the other. Different coupling conditions can be employed to model different physical/physiological phenomena.

In addition to the composite structure described above, in this work we also vary the thick structure thickness and elasticity properties to capture the presence of atheroma, a fatty plaque tissue, associated with atherosclerosis. The plaque, which is typically located within the arterial wall in a layer called tunica intima, leads to restriction in circulation, called stenosis. A cardiovascular procedure called angioplasty with stenting is often used to treat stenotic lesions. A stent, which is a metallic mesh-like tube, is anchored to the arterial wall during angioplasty to prop the stenotic arteries open. In this manuscript a stent is modeled by a change in the elastic properties of the thin structural layer where the stent struts are located. This gives rise to a net-like geometry in the thin structural layer determined by the location of the stent struts. The elastodynamics of this mesh-like structure within the thin structural layer is coupled to the elastodynamics of atheroma and blood flow via the kinematic and dynamic coupling conditions. Our approach to simulating FSI with stents is different from the classical engineering approaches, where

a stent is modeled as a single 3D elastic body [8,20,27,38,43,44,46,47,58]. Simulating slender stent struts using 3D approaches is computationally very expensive typically producing simulation results with poor accuracy due to the insufficient mesh refinement imposed by the large memory requirements associated with the use of 3D meshes to approximate slender stent struts. The approach presented in this manuscript gets around these difficulties, and we show that it provides detailed information about intramural strain distribution and intramural displacements during systolic and diastolic parts of the cardiac cycle, which are adversely affected by the presence of a stent.

The development of numerical solvers for fluid-structure interaction problems involving incompressible fluids has been a very active area of research for the past 35 years [53,52,22,26,41,30,29,32,31,19,35,33,39,40,55,54,2,59, 21,23,36,37,14,25,10]. Among the most popular techniques are the Immersed Boundary Method [53,52,22,26,41,30,29,32,31] and the Arbitrary Lagrangian Eulerian (ALE) method [19,35,33,39,40,55,54]. We further mention the Fictitious Domain Method in combination with the mortar element method or ALE approach [2,59], and the methods recently proposed for the use in the blood flow application such as the Lattice Boltzmann method [21,23,36,37], the Level Set Method [14] and the Coupled Momentum Method [25]. In relation to the FSI simulations of arterial flows, the FSI models almost exclusively assume single-layered structures that are homogeneous and isotropic to describe the mechanical properties of arterial walls, except for the recent works [5] where anisotropic polyconvex hyperelastic and anisotropic viscoelastic material models at finite strains were considered. Two types of approaches have been developed to deal with this class of multi-physics problems: a monolithic approach and a partitioned approach. In monolithic approaches the entire coupled system is solved as one monolithic system, while in partitioned approaches the coupled problem is partitioned into sub-problems, typically following the different physics in the problem, i.e., the fluid and structure sub-problems. The coupled problem is solved by iterating between the sub-problems. The first FSI model with multi-layered structures, motivated by the blood flow application, appeared in [50,10], where a partitioned scheme was designed to solve the problem [10] and to prove the existence of a weak solution to the underling FSI problem with a two-layered structure [50]. However, partitioned algorithms introduce a splitting error, and may suffer from stability issues associated with problems in hemodynamics, which are known to suffer from the so called added mass effect [12].

To solve the coupled FSI problems with multi-layered structures studied in this manuscript we use a monolithic, fully implicit method, with an Arbitray Lagrangian-Eulerian (ALE) approach employed to deal with the motion of the fluid domain [19]. Finite elements are used for spatial discretization, and finite differences for discretization in time. The resulting nonlinear monolithic system is solved using Newton's iterations, where the resulting linear system for the Jacobian is solved by GMRES with FaCSI preconditioner [17]. This method is second order accurate both in space and in time. We utilized an Open-Source library of parallel solvers called LifeV (`http://www.lifev.org/home`) as a

computational platform within which our solver was developed. This enabled us to use high resolution meshes for the simulations, totaling more than 10 million degrees of freedom, which were run on supercomputer machines at the Swiss National Supercomputing Center (CSCS) and at University of Houston's Center for Advanced Computing and Data Systems (CACDS).

The approach presented here contrasts the approaches presented in [50,10] in that: (1) the solver developed here is monolithic while the solver developed in [10] is partitioned; (2) the numerical method developed here is 2nd-order accurate in time, while the method developed in [10] is at most 1st-order accurate in time; (3) the thin structure model in the present paper is the membrane model proposed in [25,24], while the thin structure model used in [50,10] is a cylindrical Koiter shell/membrane model; (4) the numerical examples presented here are all set in 3D, while the numerical examples presented in [10] are set in 2D; (5) the numerical examples presented here include not only the 3D version of the straight two-layered tube test case studied in [10], but also an example of FSI simulation of a stenosed artery with atherosclerotic plaque (atheroma) located with the vascular wall, and an example of FSI simulation of a stenosed artery treated with a stent.

Our results show several interesting properties of FSI solutions to this class of problems. First, we confirm the findings presented in [50,10] that the presence of a thin fluid-structure interface with mass smooths-out solutions of FSI problems. As pointed out in [50,10] this is due to the fluid-structure interface inertia. See Section 4.1. As a consequence the pressure wave amplitude is dampened when compared to the pressure wave in "standard" FSI simulations in hemodynamics where arterial tissue is modeled using equations of 3D elasticity. We also found that the longitudinal wave propagation speed is increased when the thin fluid-structure interface with mass is present. The thin fluid-structure interface with mass in our model corresponds to the internal elastic laminae covered with endothelial cells comprising the inner-most layer known as tunica intima in muscular arteries. Our results implicate that the presence of this inner-most layer in muscular arteries may be responsible for damping effects in arterial pressure wave propagation, and an increase in the pressure wave propagation velocity, not captured by classical FSI models.

The results in Sections 4.2 and 4.3 show the feasibility of our model to provide novel flow information and detailed information about intramural strains in atherosclerotic arteries, and in arteries treated with stents. High intramural strains have been recently indicated as a risk factor of early-stage atherosclerosis in carotid arteries [61]. We show in Sections 4.2 and 4.3 that our simulations may be used to give a deeper insight into the details of the distribution of intramural strain. Intramural strains can be detected *in vivo* using non-invasive, ultrasound B-mode sequences [61]. They have been recently implicated as a risk factors of early-stage atherosclerosis [61]. The model presented in this manuscript could provide supplemental detailed information about intramural longitudinal tissue motion and intramural strain distribution, which could be used in conjunction with ultrasound B-mode scans as a predictive tool for an early detection of atherosclerosis [61].

2 Problem definition

2.1 Mathematical model

We consider a fluid-structure interaction problem between an incompressible, viscous fluid and an elastic structure composed of several different layers. The fluid domain, which is not known a priori, is a function of time, and is denoted by $\Omega^f(t) \subset \mathbb{R}^3$. *We assume that $\Omega^f(t)$ is a deformation of a reference domain $\hat{\Omega}^f$, usually taken as the domain at the initial time. In our applications, $\hat{\Omega}^f$ is a cylinder of length L, not necessarily symmetric, since it represents the lumen of a portion of artery.* The lateral boundary of the cylinder is assumed to be elastic and consisting of several layers: a thin layer which is in direct contact with the fluid, and a thick layer. See Figure 1. The location of the deformed thick structural layer is denoted by $\Omega^s(t)$, with the reference configuration $\hat{\Omega}^s$. The structure equations are given in Lagrangian coordinates, i.e., they are defined on the reference domain $\hat{\Omega}^s$. The thin layer, denoted by $\Gamma(t)$, which *is modeled as a membrane and* sits between the fluid and the thick elastic layer, coincides with the fluid structure interface: $\Gamma(t) = \partial\Omega^f(t) \cap \partial\Omega^s(t)$, with the reference configuration $\hat{\Gamma} = \hat{\Omega}^f \cap \hat{\Omega}^s$. The thin structure elastodynamics equations are defined on $\hat{\Gamma}$.

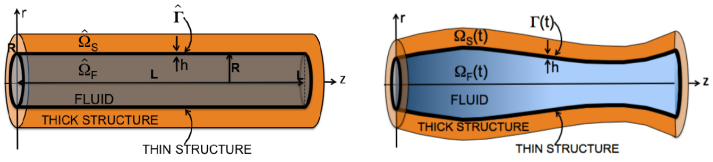

Fig. 1 Computational domain: initial configuration (left) and deformed configuration (right). *For the sake of clarity, here we show a cylindrical domain, however other configurations, like bifurcating channels, are admissible.*

The flow in $\Omega^f(t)$ is governed by the Navier-Stokes equations for an incompressible, viscous fluid:

$$\rho_f \left(\partial_t \boldsymbol{u} + (\boldsymbol{u} \cdot \nabla)\boldsymbol{u}\right) - \nabla \cdot \boldsymbol{\sigma} = \mathbf{0} \qquad \text{in } \Omega^f(t), \tag{1}$$

$$\nabla \cdot \boldsymbol{u} = 0 \qquad \text{in } \Omega^f(t), \tag{2}$$

for $t \in [0, T]$, where ρ_f is the fluid density, $\boldsymbol{u}$ is the fluid velocity and $\boldsymbol{\sigma}$ the Cauchy stress tensor. For Newtonian fluids $\boldsymbol{\sigma}$ has the following expression

$$\boldsymbol{\sigma}(\boldsymbol{u}, p) = -p\mathbf{I} + 2\mu_f \boldsymbol{\epsilon}(\boldsymbol{u}),$$

where p is the pressure, μ_f is the fluid dynamic viscosity and $\boldsymbol{\epsilon}(\boldsymbol{u}) = (\nabla \boldsymbol{u} + (\nabla \boldsymbol{u})^T)/2$ is the strain rate tensor. The fluid is driven *by the inlet and outlet boundary conditions*:

$$\boldsymbol{\sigma}\boldsymbol{n}^f_{in} = -p_{in}(t)\boldsymbol{n}^f_{in} \qquad \text{on } \Gamma^f_{in} \times (0, T), \tag{3}$$

$$\boldsymbol{\sigma}\boldsymbol{n}^f_{out} = -p_{out}(t)\boldsymbol{n}^f_{out} \qquad \text{on } \Gamma^f_{out} \times (0, T), \tag{4}$$

where $\boldsymbol{n}^f_{in}$ and $\boldsymbol{n}^f_{out}$ are the outward normals to the inlet and outlet fluid boundaries, Γ^f_{in} and Γ^f_{out}, respectively. These boundary conditions are common in blood flow modeling [3,45,51].

The structure equations are defined in Lagrangian coordinates in terms of the displacement field $\boldsymbol{d}$ of the thick structure from its given material reference configuration $\hat{\Omega}^s$, and, for the thin structure, in terms of the displacement $\boldsymbol{\eta}$ from its reference configuration $\hat{\Gamma}$. The equations governing the elastodynamics of the thick structure are given by the equations of 3D linear elasticity:

$$\rho_s \partial_{tt}\boldsymbol{d} - \nabla \cdot \boldsymbol{\Sigma}(\boldsymbol{d}) = \boldsymbol{0} \quad \text{in } \hat{\Omega}^s \times (t_0, T), \tag{5}$$

where ρ_s is the density of the thick structure, and $\boldsymbol{\Sigma}(\boldsymbol{d})$ is the first Piola-Kirchhoff stress tensor. We assume that the structure is homogeneous and isotropic. Additionally, we assume that the strain is small. Thus, we have:

$$\boldsymbol{\Sigma}(\boldsymbol{d}) = 2\mu_s \boldsymbol{\epsilon}(\boldsymbol{d}) + \lambda_s (\nabla \cdot \boldsymbol{d})\mathbf{I}. \tag{6}$$

Here, $\boldsymbol{\epsilon}(\boldsymbol{d}) = (\nabla \boldsymbol{d} + (\nabla \boldsymbol{d})^T)/2$ is the strain rate tensor, μ_s and λ_s are the Lamé constants, which are related to Young's modulus E_s and the Poisson's ratio ν_s via:

$$\mu_s = \frac{E_s}{2(1+\nu_s)}, \quad \lambda_s = \frac{E_s \nu_s}{(1+\nu_s)(1-2\nu_s)}.$$

We assume that the structure is clamped at the inlet and outlet sections Γ^s_{in} and Γ^s_{out}, and that the normal stress at the external structure boundary Γ^s_{ext} is equal to zero:

$$\boldsymbol{d} = 0 \qquad \text{on } \Gamma^s_{in/out}, \tag{7}$$

$$\boldsymbol{\Sigma}(\boldsymbol{d})\boldsymbol{n}^s_{ext} = 0 \qquad \text{on } \Gamma^s_{ext}, \tag{8}$$

where $\boldsymbol{n}^s_{ext}$ denotes the outward normal to Γ^s_{ext}.

The thin structure elastodynamics is described by a model for a linearly elastic, isotropic membrane, proposed in [25,24]. In weak form, the model is given by the following:

$$\rho_m h \int_{\hat{\Gamma}} \partial_{tt}\boldsymbol{\eta} \cdot \boldsymbol{\zeta} d\Gamma + h \int_{\hat{\Gamma}} \boldsymbol{\Pi}_\gamma(\boldsymbol{\eta}) : \nabla_\gamma \boldsymbol{\zeta} d\Gamma = \int_{\hat{\Gamma}} [\boldsymbol{\Pi}_\gamma(\boldsymbol{\eta})\boldsymbol{n}^s] \cdot \boldsymbol{\zeta} d\Gamma \quad \forall \boldsymbol{\zeta} \in \boldsymbol{V}^m, \tag{9}$$

where $[\cdot]$ on the right hand-side denotes the jump (in the normal stress across $\hat{\Gamma}$), and the test space $\boldsymbol{V}^m$ for the clamped membrane problem is given by:

$$\boldsymbol{V}^m = \{\boldsymbol{\zeta} \in (H^1(\hat{\Omega}^s))^3 |\ \boldsymbol{\zeta}|_{\hat{\Gamma}} \in (H^1(\hat{\Gamma}))^3, \boldsymbol{\zeta} = \boldsymbol{0} \text{ on } \Gamma^s_{in/out}\}. \tag{10}$$

Here $\boldsymbol{\eta} = (\eta_x, \eta_y, \eta_z)$ denotes the structure displacement, ρ_m denotes the structure density, h denotes the structure thickness, $\boldsymbol{n}^s$ is the outward normal to the solid domain $\hat{\Omega}^s$, and

$$\boldsymbol{\Pi}_\gamma(\boldsymbol{\eta}) = \frac{E_m}{1+\nu_m^2}\boldsymbol{\epsilon}_\gamma(\boldsymbol{\eta}) + \frac{E_m \nu_m}{1-\nu_m^2}\nabla_\gamma \cdot \boldsymbol{\eta}, \tag{11}$$

where $\boldsymbol{\epsilon}_\gamma(\boldsymbol{\eta}) = (\nabla_\gamma \boldsymbol{\eta} + \nabla_\gamma^T \boldsymbol{\eta})/2, \nabla_\gamma \cdot \boldsymbol{\eta} = \text{Trace}(\boldsymbol{\epsilon}_\gamma(\boldsymbol{\eta}))$ and $\nabla_\gamma(\cdot)$ denotes the surface gradient. Practically, the surface gradient can be computed as [13,9]

$$\nabla_\gamma(\boldsymbol{\eta}) = \nabla\boldsymbol{\eta}(\boldsymbol{I} - \boldsymbol{n}^s \otimes \boldsymbol{n}^s),$$

where the symbol $\otimes$ denotes the outer product and $\boldsymbol{I}$ is the identity operator. The coefficients E_m and ν_m are the membrane Young's modulus and the Poisson's ratio, respectively. This model was obtained from three-dimensional linear elasticity after assuming a thin-walled structure, a homogeneous distribution of radial stresses, and negligible bending terms. Comparisons between this model, other reduced order models and a full 3D model for fluid-structure interaction problems was investigated in [13]. The advantages of this model compared to other reduced models is that it can be easily coupled to full 3D elasticity since it captures the displacement in all three spatial directions through a weak form which is similar to full 3D elasticity.

Initially, the fluid, the thin structure and the thick structure are assumed to be at rest, with zero displacement from the reference configuration:

$$\boldsymbol{u} = \boldsymbol{0}, \quad \boldsymbol{d} = \boldsymbol{0}, \quad \boldsymbol{\eta} = 0, \quad \partial_t \boldsymbol{d} = \boldsymbol{0}, \quad \partial_t \boldsymbol{\eta} = \boldsymbol{0}, \quad \text{at } t = 0. \tag{12}$$

2.2 The ALE mapping

In order to describe the evolution of the fluid domain, we adopt an *Arbitrary Lagrangian-Eulerian* (ALE) approach [34]. Let $\hat{\Omega}^f \subset \mathbb{R}^3$ be a fixed reference domain. We consider a smooth mapping

$$\begin{aligned} \mathcal{A} \ : \ [0,T] \times \hat{\Omega}^f &\to \mathbb{R}^3, \\ \mathcal{A}(t, \hat{\Omega}^f) = \Omega^f(t), \quad &\forall t \in [0,T]. \end{aligned}$$

For each time instant $t \in [0,T]$, $\mathcal{A}$ is assumed to be a *diffeomorphism*. The domain velocity $\mathbf{w}$ is defined as

$$\mathbf{w}(t,\cdot) = \frac{d\mathcal{A}}{dt}(t, \mathcal{A}(t,\cdot)^{-1}).$$

For any sufficiently smooth function $F : [0,T] \times \mathbb{R}^3 \to \mathbb{R}$, we may define the ALE time derivative of F as

$$\partial_t F\Big|_{\hat{\mathbf{x}}} = D_t F(t, \mathcal{A}(t,\hat{\mathbf{x}})) = \partial_t F(t,\mathbf{x}) + \mathbf{w}(t,\mathbf{x}) \cdot \nabla F(t,\mathbf{x}), \text{ for } \mathbf{x} = \mathcal{A}(t,\hat{\mathbf{x}}), \ \hat{\mathbf{x}} \in \hat{\Omega}^f,$$

where D_t denotes the total derivative with respect to time. With these definitions, we can write the incompressible Navier-Stokes equations in the ALE formulation as follows:

$$\rho_f \partial_t \boldsymbol{u}\Big|_{\hat{\mathbf{x}}} + \rho_f(\boldsymbol{u} - \mathbf{w}) \cdot \nabla \boldsymbol{u} - \nabla \cdot \boldsymbol{\sigma} = \boldsymbol{0} \qquad \text{in } \Omega^f(t), \tag{13}$$

$$\nabla \cdot \boldsymbol{u} = 0 \qquad \text{in } \Omega^f(t), \tag{14}$$

for $t \in [0,T]$. Since the time derivative is now computed on the reference domain, the ALE formulation is well-suited for the time discretization.

2.3 The coupling conditions

The fluid and the composite structure are coupled via the kinematic and dynamic boundary conditions [50]:

– **Kinematic coupling conditions** describe continuity of velocity at the fluid-structure interface (no-slip condition)

$$\boldsymbol{u} \circ \mathcal{A} = \partial_t \boldsymbol{\eta} \quad \text{on } \hat{\Gamma} \times (0,T), \tag{15}$$

and continuity of the displacement (glued structures)

$$\boldsymbol{\eta} = \boldsymbol{d} \quad \text{on } \hat{\Gamma} \times (0,T); \tag{16}$$

– **Dynamic coupling condition** describes the second Newton's law of motion of the fluid-structure interface, which is loaded by the jump in the normal stress exerted by the fluid and the composite structure. The condition reads:

$$J\, \widehat{\boldsymbol{\sigma}\boldsymbol{n}^f}|_{\Gamma(t)} + \boldsymbol{\Sigma}\boldsymbol{n}^s + \boldsymbol{\Pi}_\gamma(\boldsymbol{\eta})\boldsymbol{n}^s = \boldsymbol{0} \quad \text{on } \hat{\Gamma} \times (0,T), \tag{17}$$

where J denotes the Jacobian of the transformation from Eulerian to Lagrangian coordinates, and $\widehat{\boldsymbol{\sigma}\boldsymbol{n}^f}|_{\Gamma(t)}$ denotes the normal fluid stress at the deformed fluid-structure interface, evaluated with respect to the reference configuration. Vector $\boldsymbol{n}^f$ is the outward unit normal to the deformed fluid domain.

Since equation (17) states that the load acting on the thin structure is equal to the jump in the normal stress across it, the dynamic coupling condition (17) defines the dynamics of the thin fluid-structure interface with mass, and can be written as:

$$\rho_m h \int_{\hat{\Gamma}} \partial_{tt}\boldsymbol{\eta} \cdot \boldsymbol{\zeta} d\Gamma + h \int_{\hat{\Gamma}} \boldsymbol{\Pi}_\gamma(\boldsymbol{\eta}) : \nabla_\gamma \boldsymbol{\zeta} d\Gamma = -\int_{\hat{\Gamma}} \left(J\, \widehat{\boldsymbol{\sigma}\boldsymbol{n}^f}|_{\Gamma(t)} + \boldsymbol{\Sigma}\boldsymbol{n}^s \right) \cdot \boldsymbol{\zeta} d\Gamma,$$

$\forall \boldsymbol{\zeta} \in \boldsymbol{V}^m$.

2.4 The weak formulation of the coupled problem

To write the variational formulation of problem (1)-(2), let us define the following spaces for any given $t \in [0,T)$:

$$V^f(t) = \left\{ \boldsymbol{v} : \Omega_f(t) \to \mathbb{R}^2,\ \boldsymbol{v} = \hat{\boldsymbol{v}} \circ (\mathcal{A})^{-1},\ \hat{\boldsymbol{v}} \in (H^1(\hat{\Omega}_f))^2 \right\},$$
$$Q(t) = \left\{ q : \Omega_f(t) \to \mathbb{R},\ q = \hat{q} \circ (\mathcal{A})^{-1},\ \hat{q} \in L^2(\hat{\Omega}_f) \right\},$$

The variational formulation of the fluid problem (1)-(2) reads as follows: given $t \in (0,T]$, find $(\boldsymbol{u},p) \in V^f(t) \times Q(t)$ such that $\forall (\boldsymbol{v},q) \in V^f(t) \times Q(t)$ the following holds:

$$\int_{\Omega(t)} \rho_f \left(\partial_t \boldsymbol{u} \cdot \boldsymbol{v}\right) \mathrm{d}\Omega + \int_{\Omega(t)} \rho_f \left(\left(\boldsymbol{u} \cdot \nabla\right) \boldsymbol{u} \cdot \boldsymbol{v}\right) \mathrm{d}\Omega + \int_{\Omega(t)} 2\mu_f \left(\boldsymbol{\epsilon}(\boldsymbol{u}) : \boldsymbol{\epsilon}(\boldsymbol{v})\right) \mathrm{d}\Omega - \\ - \int_{\Omega(t)} p \nabla \cdot \boldsymbol{v} \ \mathrm{d}\Omega + \int_{\Omega(t)} q \nabla \cdot \boldsymbol{u} \ \mathrm{d}\Omega = \int_{\partial\Omega^f(t)} \boldsymbol{\sigma}\boldsymbol{n}^f \cdot \boldsymbol{v} dS. \quad (18)$$

Here $\mathbf{A} : \mathbf{B}$ denotes the scalar product $\mathbf{A} : \mathbf{B} := Tr(\mathbf{A}\mathbf{B}^T)$, $\mathbf{A}, \mathbf{B} \in \mathbb{M}_3(\mathbb{R})$.

To write the weak formulation of the thick structure problem (5), we We introduce the following test function space

$$V^s = \{\boldsymbol{\varphi} \in (H^1(\hat{\Omega}^s))^3 |\ \boldsymbol{\varphi} = \mathbf{0} \text{ on } \Gamma^s_{in} \cup \Gamma^s_{out}\}, \quad (19)$$

The weak formulation of problem (5) reads as follows: Find $\boldsymbol{d} \in V^s$ such that for all $\boldsymbol{\varphi} \in V^s$ we have

$$\int_{\hat{\Omega}^s} \rho_s \left(\partial_{tt} \boldsymbol{d} \cdot \boldsymbol{\varphi}\right) \mathrm{d}\hat{\Omega} + \int_{\hat{\Omega}} 2\mu_s \left(\boldsymbol{\epsilon}(\boldsymbol{d}) : \boldsymbol{\epsilon}(\boldsymbol{\varphi})\right) \mathrm{d}\hat{\Omega} + \\ + \int_{\hat{\Omega}} \lambda_s (\nabla \cdot \boldsymbol{d})(\nabla \cdot \boldsymbol{\varphi}) \mathrm{d}\hat{\Omega} = \int_{\hat{\Omega}^s} \boldsymbol{\Sigma}\boldsymbol{n}^s \cdot \boldsymbol{\varphi} d\Gamma. \quad (20)$$

The weak formulation for the membrane problem is already given by (9). To obtain the weak formulation of the coupled problem, we introduce the following test space

$$W^f(t) = \{(\boldsymbol{v}, \boldsymbol{\varphi}, \boldsymbol{\zeta}) \in V^f(t) \times V^s \times V^m |\ \boldsymbol{v} \circ \mathcal{A} = \boldsymbol{\varphi} = \boldsymbol{\zeta} \text{ on } \hat{\Gamma} \times (0,T)\}, \quad (21)$$

which incorporates the kinematic coupling conditions (15) and (16). *For the weak formulation in this section and the energy estimate in Sec. 2.5, instead of* (3) *and* (4) *we consider inlet and outlet boundary conditions:*

$$p_+ \frac{\rho_f}{2} |\boldsymbol{u}|^2 = p_{in/out}(t) \qquad \text{on } \Gamma^f_{in/out} \times (0,T), \quad (22)$$

$$\boldsymbol{u} \times \boldsymbol{e}_z = 0 \qquad \text{on } \Gamma^f_{in/out} \times (0,T), \quad (23)$$

where $\boldsymbol{e}_z$ is the unit vector oriented like the z-axis (see Figure 1). The weak formulation of the coupled problem is then obtained by adding equations (18), (20) and (9), and by taking into account the dynamic coupling condition (17) and boundary conditions (22)-(23).

The resulting weak formulation of the coupled problem is given as follows: given $t \in (0,T]$, find $(\boldsymbol{u}, \boldsymbol{d}, \boldsymbol{\eta}, p) \in V^f(t) \times V^s \times V^m \times Q(t)$ with $\boldsymbol{u} \circ \mathcal{A} = \partial_t \boldsymbol{d} =$

$\partial_t \boldsymbol{\eta}$ on $\hat{\Gamma}$, such that for all $(\boldsymbol{v}, \boldsymbol{\varphi}, \boldsymbol{\zeta}, q) \in W(t) \times Q(t)$ the following holds:

$$\begin{aligned}
&\int_{\Omega(t)} \rho_f \left(\partial_t \boldsymbol{u} \cdot \boldsymbol{v}\right) \mathrm{d}\Omega + \int_{\Omega(t)} \rho_f \left(\left(\boldsymbol{u} \cdot \nabla\right) \boldsymbol{u} \cdot \boldsymbol{v}\right) \mathrm{d}\Omega + \int_{\Omega(t)} 2\mu_f \left(\boldsymbol{\epsilon}(\boldsymbol{u}) : \boldsymbol{\epsilon}(\boldsymbol{v})\right) \mathrm{d}\Omega - \\
&\qquad - \int_{\Omega(t)} p \nabla \cdot \boldsymbol{v} \, \mathrm{d}\Omega + \int_{\Omega(t)} q \nabla \cdot \boldsymbol{u} \, \mathrm{d}\Omega \\
&+ \int_{\hat{\Omega}^s} \rho_s \left(\partial_{tt} \boldsymbol{d} \cdot \boldsymbol{\varphi}\right) \mathrm{d}\hat{\Omega} + \int_{\hat{\Omega}^s} 2\mu_s \left(\boldsymbol{\epsilon}(\boldsymbol{d}) : \boldsymbol{\epsilon}(\boldsymbol{\varphi})\right) \mathrm{d}\hat{\Omega} + \int_{\hat{\Omega}^s} \lambda_s (\nabla \cdot \boldsymbol{d})(\nabla \cdot \boldsymbol{\varphi}) \mathrm{d}\hat{\Omega} \\
&\qquad + \int_{\hat{\Gamma}} \rho_m h \left(\partial_{tt} \boldsymbol{\eta} \cdot \boldsymbol{\zeta}\right) \mathrm{d}\Gamma + h \int_{\hat{\Gamma}} \boldsymbol{\Pi}_\gamma(\boldsymbol{\eta}) : \nabla_\gamma \boldsymbol{\zeta} d\Gamma \\
&\qquad = - \int_{\Gamma^f_{in}} p_{in}(t) \boldsymbol{v} \cdot \boldsymbol{n}^f \mathrm{d}\Gamma - \int_{\Gamma^f_{out}} p_{out}(t) \boldsymbol{v} \cdot \boldsymbol{n}^f \mathrm{d}\Gamma. \quad (24)
\end{aligned}$$

2.5 Energy estimate

To derive an energy estimate, we replace the test functions $(\boldsymbol{v}, \boldsymbol{\varphi}, \boldsymbol{\zeta}, q)$ in (24) by $(\boldsymbol{u}, \partial_t \boldsymbol{d}, \partial_t \boldsymbol{\eta}, p)$, where $(\boldsymbol{u}, \boldsymbol{d}, \boldsymbol{\eta}, p)$ is a weak solution. After a series of manipulations detailed in [49,50], and an application of Korn's and trace inequalities, one can show that the following estimate holds:

$$\frac{d}{dt}\mathcal{E}(t) + \mathcal{D}(t) \leq C \left(\|p_{in}(t)\|^2_{L^2(\Gamma^f_{in})} + \|p_{out}(t)\|^2_{L^2(\Gamma^f_{out})} \right), \quad (25)$$

where $\mathcal{E}(t)$ denotes the sum of the kinetic and the elastic energy of the coupled problem

$$\mathcal{E}(t) = \underbrace{\frac{\rho_f}{2}\|\boldsymbol{u}\|^2_{L^2(\Omega^f(t))} + \frac{\rho_s}{2}\|\partial_t \boldsymbol{d}\|^2_{L^2(\hat{\Omega}^s)} + \frac{\rho_m h}{2}\|\partial_t \boldsymbol{\eta}\|^2_{L^2(\hat{\Gamma})}}_{\text{kinetic energy}}$$

$$+ \underbrace{\mu_s \|\boldsymbol{\epsilon}(\boldsymbol{d})\|^2_{L^2(\hat{\Omega}^s)} + \frac{\lambda_s}{2}\|\nabla \cdot \boldsymbol{d}\|^2_{L^2(\hat{\Omega}^s)} + \frac{hE_m}{2(1+\nu_m^2)}\|\boldsymbol{\epsilon}_\gamma(\boldsymbol{\eta})\|^2_{L^2(\hat{\Gamma})} + \frac{hE_m\nu_m}{2(1-\nu_m^2)}\|\nabla_\gamma \cdot \boldsymbol{\eta}\|^2_{L^2(\hat{\Gamma})}}_{\text{elastic energy}},$$

and $\mathcal{D}(t)$ denotes the dissipation

$$\mathcal{D}(t) = \mu_f \|\boldsymbol{D}(\boldsymbol{v})\|^2_{L^2(\Omega^f(t))}.$$

The constant C that appears on the right-hand side of (25) depends only on the coefficients in the problem.

It was shown in [50] that the coupled fluid-multi-layered structure interaction problem, where the thin structure was modeled by the linearly elastic Koiter shell model, has a weak solution which satisfies an energy estimate corresponding to (25).

3 Discretization and monolithic solution algorithm

We present here a fully implicit scheme for the 3D fluid-multi-layered structure interaction problem (1),(2),(9),(5) for which all the nonlinearities in the problems are treated implicitly. This is in contrast with the work presented in [10] where a fluid-multi-layered structure interaction problem in 2D was solved using a partitioned scheme, called the kinematically-coupled β-scheme. Similar approaches to the one presented here but applied to fluid-thick structure interaction problems can be found in, e. g., [33,57,18,4,7,15,6,60].

We approximate the time derivatives of both the fluid and structure problems by means of second order Backward Differentation Formulas (BDF2). In space, we consider a Galerkin finite element approximation using $\mathbb{P}_2$–$\mathbb{P}_1$ Lagrange polynomials for the fluid velocity and pressure variables $\mathbf{u}$ and p respectively, and $\mathbb{P}_2$ for both the structure and fluid mesh displacement $\mathbf{d}_s$ and $\mathbf{d}_f$, respectively. Conforming meshes are considered at the fluid-structure interface.

After spatial and time discretizations, at each time step the resulting nonlinear fully-coupled system can be rewritten as:

$$\begin{pmatrix} F(\mathbf{u}^{n+1}, p^{n+1}, \mathbf{d}_f^{n+1}) & + & 0 & + I_{\Gamma^f}^T \boldsymbol{\lambda}^{n+1} & + & 0 \\ 0 & + & S(\mathbf{d}_s^{n+1}) & - I_{\Gamma^s}^T \boldsymbol{\lambda}^{n+1} & + & 0 \\ I_{\Gamma^f}\mathbf{u}^{n+1} & - & I_{\Gamma^s}/\Delta t\, \mathbf{d}_s^{n+1} & + \quad 0 & + & 0 \\ 0 & - & I_{\Gamma^s}\mathbf{d}_s^{n+1} & + \quad 0 & + & G(\mathbf{d}_f^{n+1}) \end{pmatrix} = \begin{pmatrix} \mathbf{b}_f \\ \mathbf{b}_s \\ -I_{\Gamma^s}/\Delta t\, \mathbf{d}_s^n \\ 0 \end{pmatrix}. \tag{26}$$

In (26) $\boldsymbol{\lambda}^{n+1}$ is a vector of Lagrange multipliers used to enforce the continuity of the velocities at the fluid-structure interface. *Specifically, we make use of the so-called augmented formulation (as in, e.g. [16]) wherein Lagrange multipliers are kept in the set of primary unknonws of the FSI problem. We notice that Lagrange multipliers may formally be removed from the set of unknowns of the problem by static condensation, as in [28]. However, we do not perform static condensation at this stage because it leads to additional implementation difficulties in our code library. Indeed, after partitioning the degrees of freedom into those internal and those on the fluid-structure interface, we would need to carefully manipulate the internal and interface finite element submatrices associated with each block field operator (although the finite element assembly is carried out on the whole field domain). We finally remark that although Lagrange multipliers are used in our simulation code, they do not alter the solution of the coupled FSI problem.*

On the left hand side of (26), the diagonal blocks F, S and G account for the fully-discretized fluid, multi-layered structure (sum of thick and thin layers), and geometry problems, respectively. We remark that F is nonlinear due to the convective term and the fact that the computational fluid domain

moves. The matrices I_{Γ^f} and I_{Γ^s} are the restriction of the fluid and structure vectors to the interface Γ, and are used to enforce strongly the continuity of the velocities at the fluid-structure interface, and the geometry adherence. Their transposes account for the continuity of the normal stresses, which is imposed in weak form.

We solve the monolithic nonlinear problem (26) by using the Newton's method. At each time step, the generic $k+1$ iteration of the Newton's algorithm applied to (26) reads: starting from an approximation of $\mathbf{X}_k^{n+1} = (\mathbf{u}_k^{n+1}, p_k^{n+1}, \mathbf{d}_{s,k}^{n+1}, \boldsymbol{\lambda}_k^{n+1}, \mathbf{d}_{f,k}^{n+1})^T$, we compute the residual $\mathbf{R}_k^{n+1} = (\mathbf{r}_{F,k}^{n+1}, \mathbf{r}_{S,k}^{n+1}, \mathbf{r}_{C,k}^{n+1}, \mathbf{r}_{G,k}^{n+1})^T$:

$$\mathbf{R}_k^{n+1} = \begin{pmatrix} \mathbf{b}_f \\ \mathbf{b}_s \\ -I_{\Gamma^s}/\Delta t \mathbf{d}_{s,k}^n \\ 0 \end{pmatrix} - \begin{pmatrix} F(\mathbf{u}_k^{n+1}, p_k^{n+1}, \mathbf{d}_{f,k}^{n+1}) + I_{\Gamma^f}^T \boldsymbol{\lambda}_k^{n+1} \\ S(\mathbf{d}_{s,k}^{n+1}) - I_{\Gamma^s}^T \boldsymbol{\lambda}_k^{n+1} \\ I_{\Gamma^f} \mathbf{u}_k^{n+1} - I_{\Gamma^s}/\Delta t \, \mathbf{d}_{s,k}^{n+1} \\ -I_{\Gamma^s} \mathbf{d}_{s,k}^{n+1} + G(\mathbf{d}_{f,k}^{n+1}) \end{pmatrix}. \tag{27}$$

Then, we compute the Newton correction vector $\delta\mathbf{X}_k^{n+1} = (\delta\mathbf{u}_k^{n+1}, \delta p_k^{n+1}, \delta\mathbf{d}_{s,k}^{n+1}, \delta\boldsymbol{\lambda}_k^{n+1}, \delta\mathbf{d}_{f,k}^{n+1})^T$ by solving the Jacobian linear system

$$\mathbf{J}_{FSG} \, \delta\mathbf{X}_k^{n+1} = -\mathbf{R}_k^{n+1}, \tag{28}$$

where $\mathbf{J}_{FSG}$ is the exact FSI Jacobian matrix [13]. Finally, we update the solution, i.e.

$$\mathbf{X}_{k+1}^{n+1} = \mathbf{X}_k^{n+1} + \delta\mathbf{X}_k^{n+1}.$$

We stop the Newton iterations when $\|\mathbf{R}_k^{n+1}\|_\infty / \|\mathbf{R}_0^{n+1}\|_\infty \leq \epsilon$, where $\|\mathbf{R}_0^{n+1}\|_\infty$ is the discrete L^∞-norm of the residual at the first Newton iteration and ϵ is a given tolerance. Linear system (28) is solved using the GMRES method preconditioned by FaCSI [17].

4 Numerical results

4.1 Pressure wave propagation through a straight flexible cylinder

Our goal in this first test is to understand the impact of the thin layer thickness on the solution of the coupled problem. This is interesting for several reasons. It was shown in [50] and in [10] that as the thickness of the thin layer approaches zero, the solution of the fluid-thin-thick structure interaction problem converges to the solution of the FSI problem with only one thick structure. This was first shown in [50] analytically on a simplified, linear problem where the fluid-structure coupling was considered to happen across a fixed fluid-structure interface. It was then shown numerically in [10] that this was true for a fully nonlinear FSI problem set in 2D. Moreover, it was shown that the presence of a thin structure with mass at the fluid-structure interface smooths-out the solution of the FSI problem with multi-layered structures.

This "regularizing" property was not due to the viscosity induced dissipation (since both structures were strictly elastic), but due to *inertia* of the thin fluid-structure interface with mass. This finding has many important practical implications, including the understanding of the pressure wave propagation in arterial walls, which are composed of several different layers, with a thin elastic layer (elastic lamina) covered with endothelial cells that are in direct contact with blood flow. This thin elastic lamina covered with endothelial cells plays the role of the thin elastic structure with mass, located at the fluid-multi-layered structure interface, studied in the present paper. Thus, we consider a test case which consists of simulating the propagation of a pressure wave in a fluid-filled straight elastic pipe, and study the behavior of its solution as the thickness of the thin structure converges to zero.

For this purpose, we consider the fluid domain to be a cylinder of radius $R_{in} = 0.5$ cm, length $L = 5$ cm, with an elastic lateral boundary consisting of two layers: thin and thick, where the thin layer is in direct contact with fluid flow and serves as a fluid-structure interface with mass. Let h be the thickness of the thin layer and H the thickness of the thick layer. With the monolithic algorithm presented in Section 3, we solve a sequence of FSI problems in 3D where h decreases while the total thickness of the composite structure is kept constant, i.e. such that $h+H = h_{tot} = 0.1$ cm. We consider h equal to $80\%, 60\%, 40\%, 20\%, 10\%, 5\%$ and 0% of the total thickness h_{tot} and set H accordingly, i.e. $H = h_{tot} - h$. The results obtained using a single (thick) layer model for the structure correspond to the case $h = 0$ cm. The coupled fluid-structure system is initially at rest. At the fluid domain inlet we apply a constant normal stress $\boldsymbol{\sigma} \cdot \mathbf{n}^f_{in} = 1.33 \times 10^4$ dyne/cm^2 for a given time interval $t \in (0, 0.003)$ s, and then set the normal stress equal to zero. At the fluid domain outlet and at the outer structure wall, a stress-free boundary condition is imposed. Homogeneous Dirichlet boundary conditions, i.e., zero displacement, are enforced at both ends of the vessel wall. All physical parameters for the fluid and composite structure used in the simulations are given in Table 1. Notice that since we are interested in understanding the behavior of the solution as the thin layer thickness tends to zero (i.e. as the two-layer model tends to the single layer model), in this preliminary example we considered the same density, Poisson ratio and Young's modulus for both the thin and thick layers.

	Parameter	**Value**	**Parameter**	**Value**
Fluid	Fluid density, ρ_f	1 g/cm^3	Dynamic viscosity, μ_f	0.03 g/cm s
Thin wall	Density, ρ_m	1.2 g/cm^3		
	Poisson ratio, ν_m	0.3	Young's modulus, E_m	$3 \cdot 10^6$ dyne/cm^2
Thick wall	Density, ρ_s	1.2 g/cm^3		
	Poisson ratio, ν_s	0.3	Young's modulus, E_s	$3 \cdot 10^6$ dyne/cm^2

Table 1 Physical parameters used for the fluid and the double-layered structure.

The inlet boundary condition used initiates a pressure wave propagating through the fluid domain, which is simulated over the time interval $[0, 0.01]$ s using the time step $\Delta t = 5 \times 10^{-4}$ s. We report in Table 2 the information associated with the fluid and structure meshes used for the simulation while in Table 3 we show the corresponding numbers of Degrees of Freedom (DoF).

	Number of vertices	Number of elements
Fluid mesh	14784	78390
Structure mesh	8712	34320

Table 2 Details of the fluid and structure meshes used for Example 4.1.

Fluid Dof	Structure DoF	Coupling DoF	Geometry DoF	Total
348441	172920	34056	333657	889074

Table 3 Number of degrees of freedom for the simulation of the pressure wave propagation in a flexible straight cylinder. The number of fluid DoF is the sum of the velocity and the pressure DoF.

In Figure 2 we show the radial component of displacement of the fluid structure interface for different values of h at times $t = 0.002, 0.004, 0.006, 0.008$ s. We notice that as the thin structure thickness h tends to 0, the solution of the fluid-multi layered structure interaction problem converges to the solution of the fluid-thick structure interaction problem, which corresponds to the solution with the largest amplitude.

We observe that the thin layer has a smoothing effect on the interface displacement. In fact, the larger the value of h, the smaller the value of the (positive and negative) peak radial displacements, and the milder the gradient of the radial displacement along the z-coordinate. Such regularizing effect of the thin layer inertia is also visible from Figure 3, where we report a visualization of the structure displacement at time $t = 0.008$ s for different values of h. This is in agreement with the recent theoretical results, presented in [48], which show that the presence of a thin interface with mass between a parabolic and a hyperbolic problem regularizes the solution of the coupled problem. Furthermore, it was shown in [10] that as the thickness h of the thin fluid-structure interface with mass converges to zero, the solution of the coupled FSI problem in which the combined structure thickness is kept constant, converges to the solution of the FSI problem with only one (thick) structure of finite thickness H. To avoid dealing with the ALE mapping, the proof in [10] was obtained for the FSI problem in which the fluid domain was kept fixed (linearized FSI problem). This still captures the main features of the coupled FSI problem related to the convergence $h \to 0$.

From Figures 2 and 3 we also see that the larger the value of h, the faster the pressure wave propagates in the fluid domain.

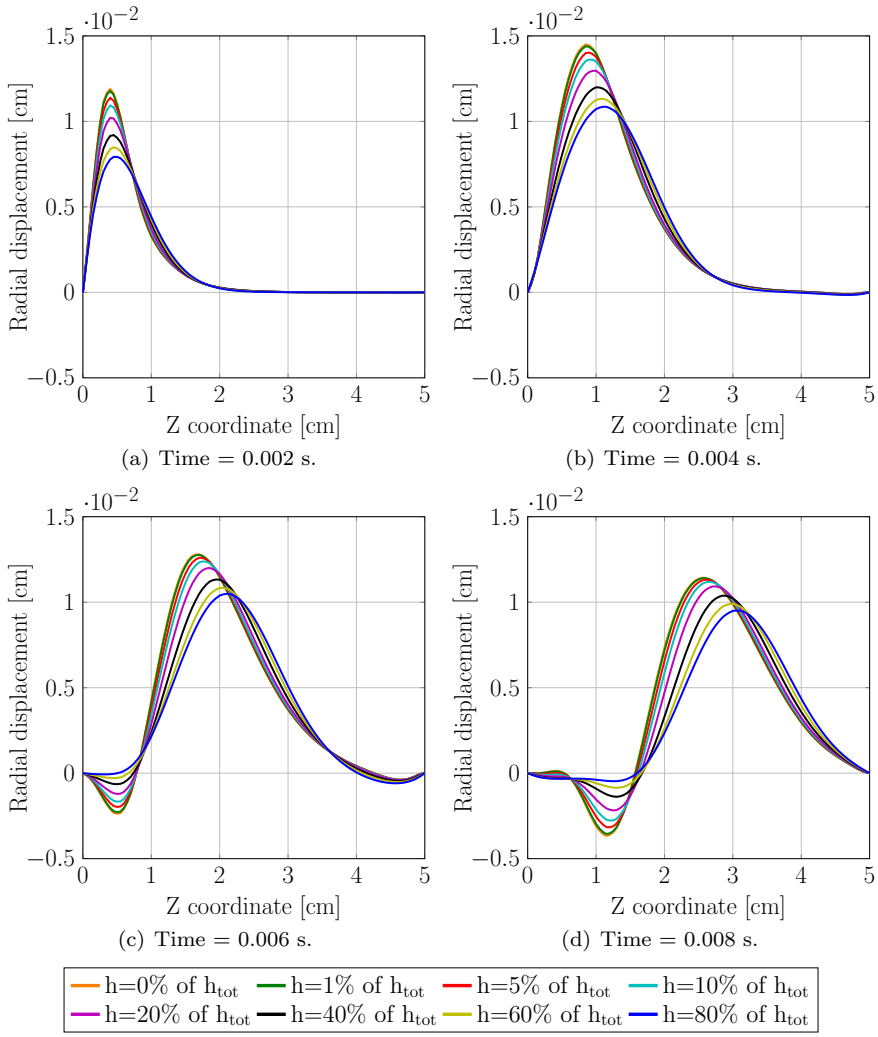

Fig. 2 Radial component of interface displacement for different values of the thin structure thickness h at times: (a) $t = 0.002$ s, (b) $t = 0.004$ s, (c) $t = 0.06$ s, (d) $t = 0.08$ s. The legend is reported at the bottom of the figure.

We observed that the presence of the thin layer does not cause an increase in the average number of Newton iterations per time step. In our simulations the number of Newton iterations was equal to 3, regardless of the value of h. Similarly, we observed that the average number of GMRES iterations to solve the linear system (28) is independent of h. In our simulations the number was roughly equal to 28.

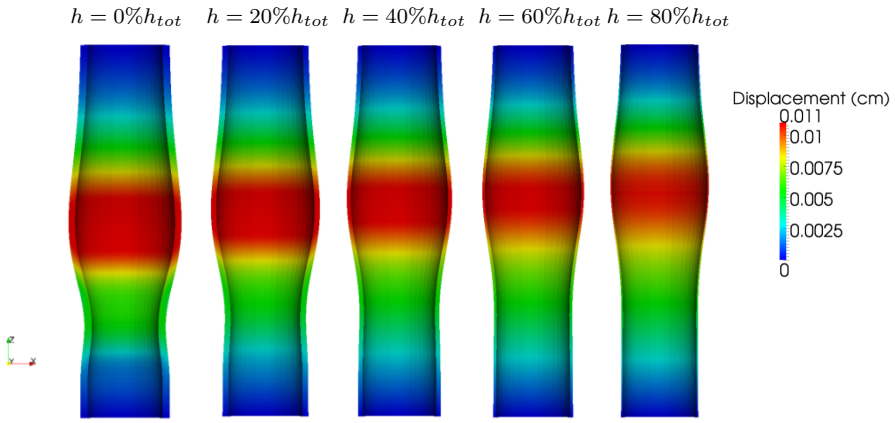

Fig. 3 Displacement of the solid visualized on a longitudinal clip of the domain at time $t = 0.008$ s for different values of h. The deformation is magnified by a factor 15 for visualization purposes.

4.2 Diseased artery

We consider an artery affected by the presence of atheroma, an accumulation of fatty material in the tunica intima of the arterial walls, typically associated with atherosclerosis. The degenerative accumulated material of atheroma protrudes into the lumen, narrowing it. This is known as a stenotic lesion. The location of atheroma is always in the tunica intima, between the endothelium lining and the smooth muscle tunica media of the arterial wall. See Figure 4.

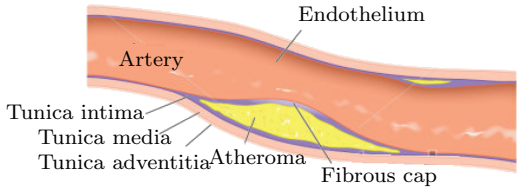

Fig. 4 Schematic representation of an atheroma.

Our composite structure model is particularly suited to simulate the behavior of such composite structures. The thin layer of the tunica intima (with the fibrous cap) that is in direct contact with blood flow is modeled by the thin elastic structure layer (elastic membrane) in our multi-layered structure model. The rest of the arterial wall is modeled by the equations of 3D elasticity, where the presence of atheroma is captured by the change in the elasticity parameters, which are chosen to be "stiffer" (higher Young's modulus) in the atheroma region (see Cases 2 and 4 below). Table 4 shows the parameter values for the simulation. The computational geometry of the vessel lumen (the

	Parameter	Value	Parameter	Value
Fluid	Fluid density, ρ_f	1.055 g/cm^3	Dynamic viscosity, μ_f	0.04 g/(cm s)
Thin wall	Density, ρ_m Poisson ratio, ν_m	1.055 g/cm^3 0.4	Young's modulus, E_m	$4 \cdot 10^6$ dyne/cm^2
Healty thick wall	Density, ρ_s Poisson ratio, ν_s	1.055 g/cm^3 0.4	Young's modulus, E_s	$4 \cdot 10^6$ dyne/cm^2
Atheroma	Density, ρ_a Poisson ratio, ν_a	1.055 g/cm^3 0.4	Young's modulus, E_a	$5.02 \cdot 10^6$ dyne/cm^2

Table 4 Physical parameters used for the simulation of the diseased artery.

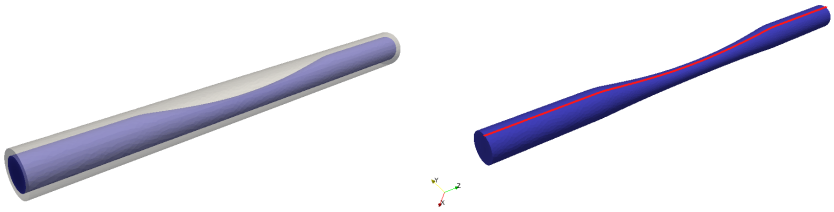

(a) Computational geometry (b) Fluid domain

Fig. 5 (a) Computational domain for the diseased artery: the fluid domain is in blue and the structure domain is in gray. (b) Fluid domain with a red curve showing where on the fluid-structure interface the displacement was postprocessed. In subfigure (b) the orientation of the axes is also reported. The direction of the flow is aligned with the z-axis.

area occupied by blood), showing the protrusion of the atheroma, is shown in Figure 5 (a). The blue region is the vessel lumen, while the arterial wall, modeled by as a composite thin-thick structure, is shown in grey. The radius of the artery away from the atheroma is $R = 0.18$ cm. The thick layer of the vessel wall has thickness $H = 0.07$ cm where it is healthy, while in the atheroma region the thickness is increased up to the value of 0.188 cm, giving rise to around 60% stenosis. The computational domain is 6 cm long.

We are interested in studying how the numerical results obtained using our two-layered structure model compare with the results obtained using a single-layered structure model (thick structure only). We are also interested in exploring how the flow and displacement are affected by the change in the structure parameters by comparing solutions obtained with uniform structure parameters versus solutions obtained with varying structure parameters in the atheroma region.

We consider four cases:

1. Fluid interacting only with one thick layer with uniform Young's modulus E_s.
2. Fluid interacting only with one thick layer with variable Young's modulus: E_s in the healthy region, E_a in the atheroma region.
3. Fluid interacting with a two-layered structure with the thick layer as in case 1 and a thin layer with Young's modulus E_m.

4. Fluid interacting with a two-layered structure with the thick layer as in case 2 and a thin layer with Young's modulus E_m.

The parameters values E_s, E_a, and E_m are given in Table 4. The thickness of the thin layer in cases 3 and 4 is set to $h = 0.01$ cm.

We impose non-homogeneous Neumann conditions (normal stress) at the inflow and outflow boundaries, using physiologic pressures taken from measurements by Marques et al. [42]. See Figure 6. These measurements refer to

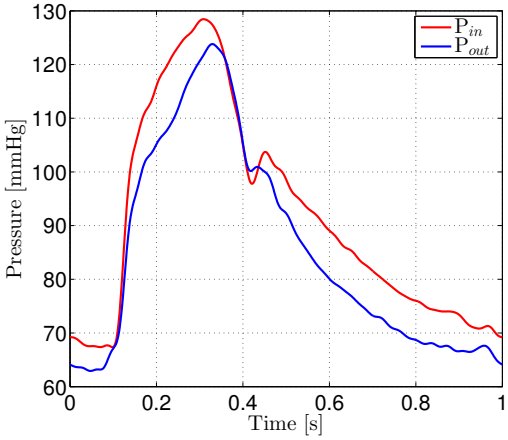

Fig. 6 Inflow and outflow pressures used in our simulations.

the trans-stenotic pressure gradient in coronary arteries (left anterior descending (LAD)). The length of the stenotic region was not provided in [42]. As in the previous subsection, homogeneous Dirichlet boundary conditions are enforced at both ends of the vessel wall (clamped structure) and a homogeneous Neumann condition is chosen for the outer structure surface (zero external normal stress). The simulations are started from fluid at rest and a couple of cycles are run before post-processing the results in order to be sure that time periodic flow is established. In Table 5 we report the number of vertices and

	Number of vertices	Number of elements
Fluid mesh	70167	330909
Structure mesh	86298	374752

Table 5 Details of the fluid and structure meshes used for the diseased artery simulation.

elements of the fluid and structure meshes used in the simulations. We used $\mathbb{P}_2$–$\mathbb{P}_1$ finite elements for the fluid velocity and pressure variables, $\mathbb{P}_2$ for the structure displacement and $\mathbb{P}_2$ for the ALE. In Table 6 we report the number of Degrees of Freedom (DoF) associated to the fluid and structure meshes used.

We remark that even though the pressure data we used in our simulations is physiologic, one should not expect that our simulations provide physiologic flow velocities or displacements in a stenosed LAD corresponding to the studies reported in [42]. Not enough data was provided in [42] to recreate the corresponding numerical simulations. Hence, this example was designed to illustrate, under the physiologic pressure wave forms, what is the influence of different structure models and structure coefficients on the solutions of the underlying FSI problem.

Fluid Dof	Structure DoF	Coupling DoF	Geometry DoF	Total
1829079	1781235	329352	1498170	5437836

Table 6 Number of degrees of freedom for the diseased artery simulation. The number of fluid DoF is the sum of the velocity and the pressure DoF.

We investigate the behavior of velocity, of the fluid-structure interface displacement, and of the 3D thick structure displacement throughout the entire structure, under the flow conditions described above, and for the four cases of structure models described above.

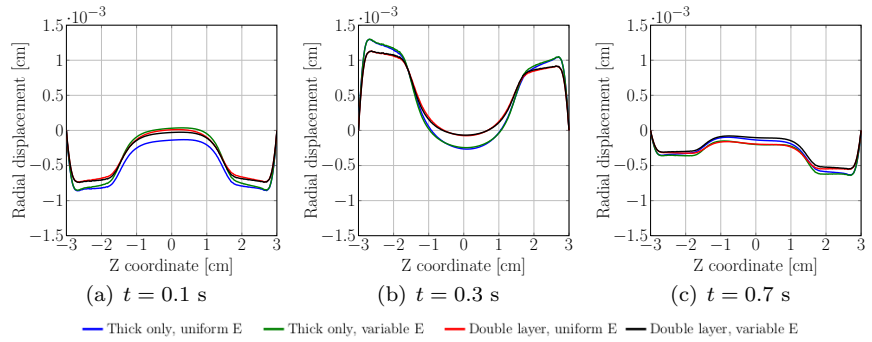

Fig. 7 Radial component of the fluid-structure interface displacement along the red line in Figure 5(b) for cases 1 (only thick, uniform E), 2 (only thick, variable E), 3 (double layer, uniform E), and 4 (double layer, variable E) at times: (a) $t = 0.1$ s, (b) $t = 0.3$ s, (c) $t = 0.7$ s.

Figures 7 and 8 show the radial component of the fluid-structure interface displacement and radial velocity of the interface along the cut of the computational domain shown in red line in Figure 5(b). The four structure models listed under 1, 2, 3, and 4 above, are depicted in four different color lines. Three different snap-shots during one cardiac cycle are shown in both figures. In Figure 7 we observe that the atheroma region displaces much less than the surrounding tissue, as expected. In particular, at time $t = 0.1$ s, at the beginning of the cardiac cycle when the pressure gradient between the inlet

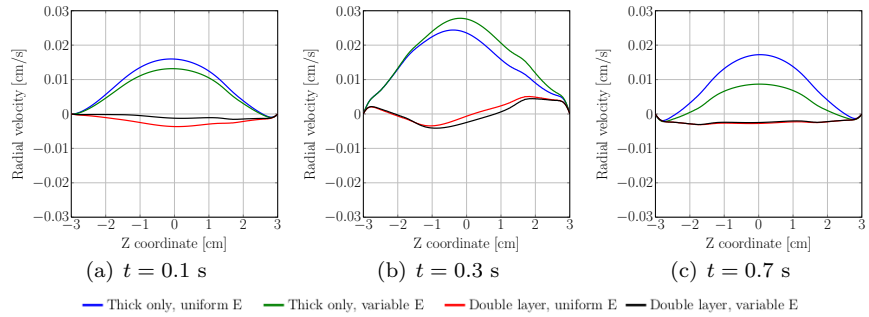

Fig. 8 Radial component of the fluid-structure interface velocity along the red line in Figure 5(b) for cases 1 (only thick, uniform E), 2 (only thick, variable E), 3 (double layer, uniform E), and 4 (double layer, variable E) at times: (a) $t = 0.1$ s, (b) $t = 0.3$ s, (c) $t = 0.5$ s, (d) $t = 0.7$ s.

and outlet is negative, the healthy part of the structure is pulled into the lumen, while at $t = 0.3$ s, which corresponds to the systolic peak, the healthy portion of the artery is inflated relative to the atheroma region, with high displacement gradients, especially near the proximal site of the atheroma. See Figure 7 (b). When comparing the four different models, shown in different color lines in Figure 7, we see that the largest displacements occur when only one thick structure is used to model the arterial wall, corresponding to the blue and green lines in all the figures, indicating 20% larger maximal displacement in Figure 7 (b). This is consistent with the findings presented in the first example, see Section 4.1. Lower amplitude of displacement in models with two structural layers is attributed to the smoothing effects of the fluid-structure interface inertia.

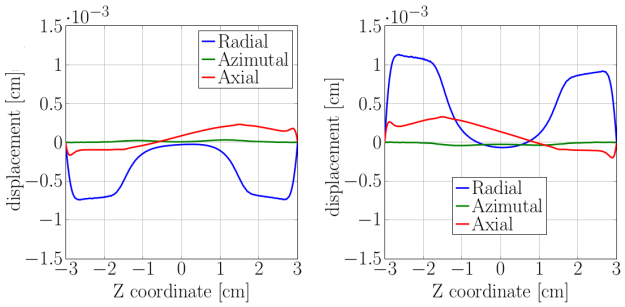

Fig. 9 Case 4 (double layer, variable E): Radial, azimuthal, and axial components of the fluid-structure interface displacement along the red line in Figure 5(b) at time (a) $t = 0.1$ s and (b) $t = 0.3$ s.

The smoothing effect of the double-layered structure is even more evident in the radial velocity plots in Figure 8. We see, among other things,

a significantly smaller radial velocity for the double-layer model due to the fluid-structure interface inertia. Figure 8(b) also shows a significantly smaller interface radial velocity for the thick structure model with variable Young's modulus reflecting the presence of atheroma in the thick structure model. This shows that the choice of a particular structure model to simulate the behavior of FSI solutions in hemodynamics, significantly influences the solution itself. We remind that vascular tissue is a composite structure made of several different layers. Thus, we believe that multi-layered structure models more closely approximate the true composite, multi-layered structure of arterial walls, and should be preferred in hemodynamics simulations over single structure models. For the two-layered structure model with variable Young's modulus, i.e.,

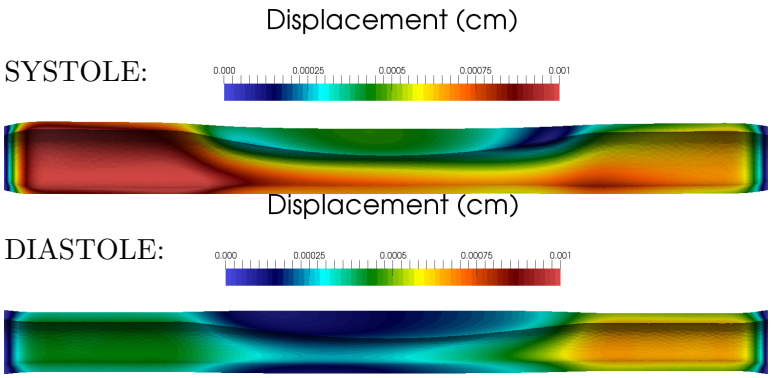

Fig. 10 Case 4 (double layer, variable E): clip of the structure along the red line in Figure 5(b) colored with the displacement magnitude and showing the structure deformation magnified by a factor 50 at time (a) $t = 0.25$ s (systole) and (b) $t = 0.75$ s (diastole). This figure shows how our model captures displacement throughout the thickness of the entire structure. Large displacement during systole is observed at the site proximal to the atheroma region, while during diastole, larger displacement is observed downstream from the atheroma region. The displacement of the atheroma region is very low throughout the entire cardiac cycle. Large strains can be expected at the proximal and distal ends of the atheroma, indicated by the large color gradients in the figure.

case 4, we further investigated the behavior of the radial, azimuthal, and axial components of displacement. In Figure 9 we report the three components of the fluid-structure interface displacement at the beginning of the cardiac cycle, i.e., at $t = 0.1$ s, and at the systolic peak, i.e., at $t = 0.3$ s. We see that the radial and longitudinal displacements are of the same order of magnitude, while the azimuthal component of displacement is much smaller. We also see that at the systolic peak, the axial component of displacement drops significantly through the atheroma region.

Finally, we report in Figure 10 the 3D structure displacement magnitude for the case of a double-layered structure with variable Young's modulus (case 4) on the clip of the structure domain along the red line in Figure 5(b) at two different times: one corresponding to the systolic peak, and one to mid diastole. The structure deformation in Figure 10 is magnified by a factor 50.

We see significant change in displacement in the atheroma region where displacement magnitude is small, with high displacement gradients in the healthy tissue adjacent to the atheroma region, and higher displacement magnitude, especially during systole, in the healthy tissue away from the atheroma. The high displacement gradients, shown in Figure 10 (a) by the change in the color of displacement magnitude, indicate high intramural strains. High intramural strains have been recently indicated as a risk factor of early-stage atherosclerosis in carotid arteries [61]. We have shown with this example that our simulations may be used to give a deeper insight into the details of the distribution of intramural strain that can be detected *in vivo* using non-invasive, ultrasound B-mode sequences, and eventually be used as a predictive tool for an early detection of atherosclerosis [61].

In conclusion, our results indicate that while the differences in structure displacements are not drastic for the four different structure models, the difference in the radial component of interface velocity between the four different cases is significant, indicating the smoothing properties of inertia of the thin fluid-structure interface with mass. Furthermore, our results show that the magnitude of longitudinal displacement of the fluid-structure interface, although smaller, is still comparable to the magnitude of radial displacement, which contrasts the assumptions typically used in the derivation of 1D reduced FSI models from the equations of linear elasticity [11]. Finally, we showed that the composite structure model discussed in this paper enables clear identification of distribution of 3D structure displacement and displacement gradients, indicating the regions within the arterial wall where high strains in healthy artery occur due to the presence of atheroma, which may be a pre-cursor for a further growth of atherosclerotic lesions.

4.3 Diseased artery treated with a stent

We consider fluid-structure interaction between blood flow and a stenotic artery treated with a stent. A stent is a metallic mesh-like tube which is used to prop the diseased arteries open. A fully expanded stent ideally recovers the original vessel lumen, while it pushes the fatty deposits in the atheroma region against the arterial walls. As a result, the stenotic artery treated with a stent protrudes outwards to accommodate the presence of the atheroma in the arterial wall, while at the same time keeping the diameter of the treated vessel within the normal range. Our computational geometry of the arterial wall, simulating the situation described above, is shown in Figure 11.

The gray region in Figure 11 corresponds to the normal arterial tissue. The red region shows the presence of the atheroma within the arterial wall, where the Young's modulus of elasticity is higher, and is given in Table 7. The stent, shown in blue color in Figure 11 (b), is located in the thin structural layer, and is modeled by the significantly higher Young's modulus where the stent struts are located. We set the stent Young's modulus to $E_{st} = 2.43 \times 10^{11}$ Pa, which corresponds to L-605 cobalt-chromium alloy. This is a commonly used

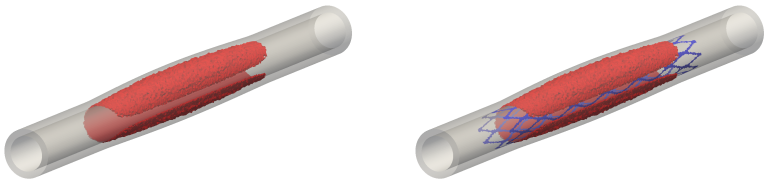

(a) Asymmetric atheroma. (b) Atheroma treated with a stent.

Fig. 11 Structure geometry with visualization of the plaque, shown in red in panel (a), and with an implanted stent, shown in blue in panel (b).

	Parameter	**Value**	**Parameter**	**Value**
Fluid	Fluid density, ρ_f	1.055 g/cm^3	Dynamic viscosity, μ_f	0.04 g/cm s
Thin wall	Density, ρ_m	1.055 g/cm^3		
	Poisson ratio, ν_m	0.4	Young's modulus, E_m	$4 \cdot 10^6$ dyne/cm^2
Stent	Density, ρ_{st}	8.5 g/cm^3		
	Poisson ratio, ν_{st}	0.31	Young's modulus, E_{st}	$2.43 \cdot 10^{12}$ dyne/cm^2
Healthy thick wall	Density, ρ_s	1.055 g/cm^3		
	Poisson ratio, ν_s	0.4	Young's modulus, E_s	$4 \cdot 10^6$ dyne/cm^2
Atheroma	Density, ρ_{a}	1.055 g/cm^3		
	Poisson ratio, ν_{a}	0.4	Young's modulus, E_{a}	$5.02 \cdot 10^6$ dyne/cm^2

Table 7 Physical parameters used for simulation of the diseased artery with stent implanted.

material in stent manufacturing [56]. We assume that the stent struts are 0.12 mm thick [56] and set the thickness of the thin layer to 0.12 mm. All the other physical parameters for the simulation are reported in Table 7.

	Number of vertices	Number of elements
Fluid mesh	200515	1034917
Structure mesh	126635	524092

Table 8 Details of the fluid and structure meshes used.

Fluid Dof	Structure DoF	Coupling DoF	Geometry DoF	Total
4666354	2560404	204916	4465839	11897513

Table 9 Number of degrees of freedom for the simulation of the diseased artery treated with a stent. The number of fluid DoF is the sum of the velocity and the pressure DoF.

Simulating slender stent struts using 3D approaches is computationally very expensive, typically producing simulation results with poor accuracy due

to the insufficient mesh refinement imposed by the large memory requirements associated with the use of 3D meshes to approximate the struts. Since the stent struts' thickness is small compared to the stent length, modeling stents by changing the stiffness coefficients in the thin structure model of thickness h, in places where the stent struts are located, provides a computationally less expensive way of simulating stents. This manuscript is the first work in which a stent is modeled this way, and is coupled to the elastodynamics of the thick structure, i.e., the rest of the arterial wall, via the kinematic and dynamics coupling conditions (15), (16), (17).

We impose the same boundary conditions as in Section 4.2. Again, the simulations are started from fluid at rest and a couple of cycles are run before post-processing the results in order to be sure that time periodic flow is established. In Table 8 we report the number of vertices and elements for the fluid and structure meshes used in the simulations. In Table 9 we show the number of degrees of freedom used in our numerical simulation. Figure 12 shows the

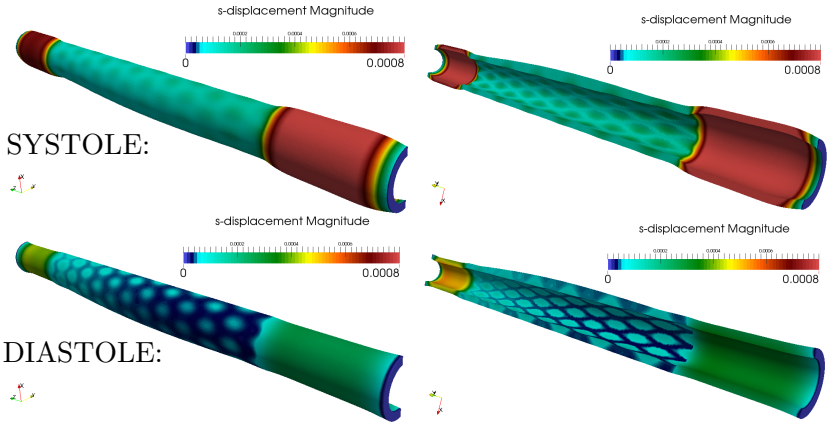

Fig. 12 Displacement magnitude at $t = 0.3$ s (systole) and $t = 0.7$ s (diasole). The exterior (left) and interior (right) views of the structure displacement are shown. The structure deformation is magnified by a factor of 50. The direction of flow is from right to left.

structure displacement magnitude at the systolic peak ($t = 0.3$ s) and at diastole ($t = 0.7$ s). The structure deformation is magnified by a factor 50. The flow direction in Fig. 12 is from right to left. At both times and both on the inner and outer structure surfaces, the displacement magnitude clearly reveals the presence of the stent. In fact, the structure displacement is smaller where the stent is located, as expected given the high stiffness of the stent material (see Table 7). One can observe in Fig. 12 (b) and (d) that the displacement magnitude decreases within the arterial wall in the radial direction, starting from the luminal region and going toward the outer wall. In fact, Figure 13 clearly shows high gradients in magnitude of displacement surrounding the stent struts at three different arterial cross-sections (proximal, central, and distal). This indicates high intramural strains in the area where the stent is

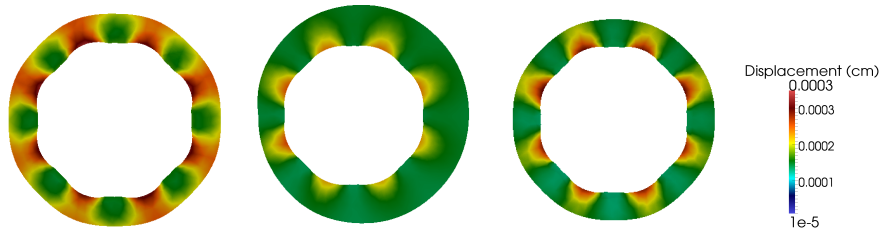

(a) proximal, $t = 0.3$ s (b) central, $t = 0.3$ s (c) distal, $t = 0.3$ s

Fig. 13 Stented artery: displacement magnitude at the *section corresponding to the proximal end, center, and distal end of the stent* at the systolic peak $t = 0.3$ s (first row). The structure deformation is magnified by a factor 50.

located, which may be responsible for an onset of a cascade of events leading to in-stent restenosis [1, 43].

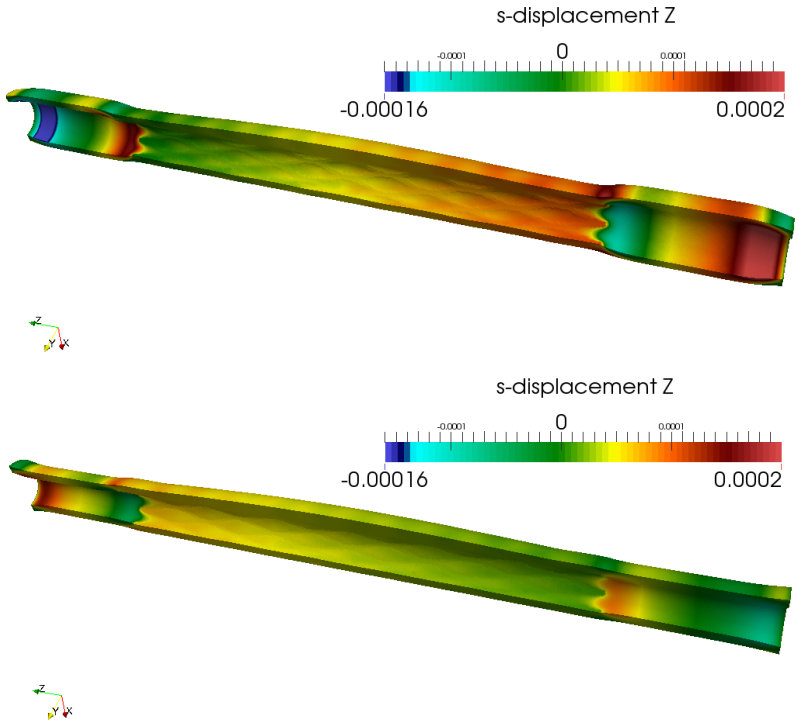

Fig. 14 Axial component of the structure displacement viewed from the interior of fluid domain at time $t = 0.3$ s (top) and $t = 0.7$ s (bottom). The structure deformation is magnified by a factor 50. The direction of flow is oriented like the z-axis.

We further investigated the longitudinal (axial) displacement throughout the arterial wall to see how the presence of a stent influences the longitu-

dinal displacement. Figure 14 reports the axial component of the structure displacement on a clip of the structure domain at systole ($t = 0.3$ s) and at diastole ($t = 0.75$ s). The structure deformation is magnified by a factor of 50. The cool color shades (green-cyan-blue-purple) denote compression, while the warm color shades (yellow-orange-red) denote stretching.

We first notice that the axial component of displacement is non-negligible, as was the case with only atheroma, studied in Section 4.2. In fact, the maximum axial displacement in absolute value is 0.0002 cm, while the maximum overall magnitude of displacement is 0.0008 cm (see Fig. 12). More importantly, Figure 14 shows that large longitudinal displacements occur at the proximal and distal ends of the stent, and at the inlet (in systole) and outlet of the tube (in diastole). The large displacements near the inlet and outlet of the tube are the artifacts of the homogeneous boundary conditions on the structure displacement (fixed ends) and are not physiological. However, the large displacements and displacement gradients near the proximal and distal ends of the stent are likely physiologically relevant. In particular, we see that in systole, the healthy tissue near the proximal end of the stent is significantly compressed in the longitudinal direction toward the stent, due to the presence of the rigid stent, which is obstructing the tissue movement, while in diastole, the healthy tissue near the distal end of the stent is significantly stretched in the direction of flow. One can observe particularly large displacement gradients near both ends of the prosthesis, which may, as mentioned earlier, be a pre-cursor for development of neo-intimal hyperplasia due to the chronic tissue damage.

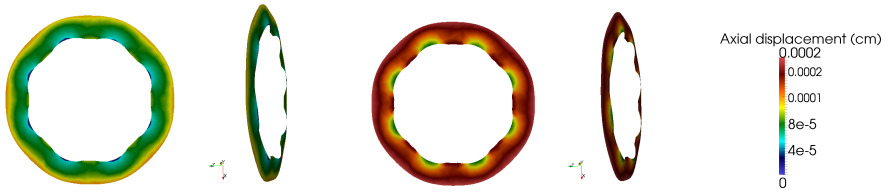

(a) $t = 0.3$ s, front (b) $t = 0.3$ s, side (c) $t = 0.35$ s, front (d) $t = 0.35$ s, side

Fig. 15 Axial component of structure displacement at the *section corresponding to the proximal end of the stent* at time $t = 0.3$ s (a) front view and (b) side view, and $t = 0.35$ s (c) front view and (d) side view. The structure deformation is magnified by a factor 50.

We conclude this section by showing how axial displacement varies intramurally, i.e., throughout the structure thickness. Figure 15 shows the axial displacement at the proximal end of the stent just before the maximum axial displacement in systole ($t = 0.3$ s), and at the maximum axial displacement ($t = 0.35$ s). Two views are shown: the frontal view and the side view. From the side views, we can see how the cross-section, initially in plane, deforms out of plane.

The figure shows that at $t = 0.3$ s, the stent struts undergo no axial displacement, while the tissue in-between the struts and throughout the thick wall, stretch in the direction of flow, showing a "skirt" pattern along the lumen circumference, i.e., at the fluid-structure interface. At $t = 0.35$ s the stent struts start "catching up", producing non-zero axial displacement following the motion of the fluid. The stent strut displacement is, however, still smaller than that of the surrounding tissue, producing again a skirt pattern in the azymuthal direction within the stent. Figure 15 clearly shows high intramural axial displacement gradients, contributing to the events associated with in-stent restenosis.

This example shows the feasibility of our model to provide various novel pieces of information that can be used to study the interaction between blood flow and fully expanded stents implanted within stenotic lesions.

5 Conclusions

This work presents a first monolithic computational fluid-composite structure interaction model designed to capture the interaction between blood flow and a diseased multi-layered arterial wall treated with a vascular prostheses called a stent. The model can capture the presence of atheroma, a fatty material that forms plaque in arteries, the multi-layered structure of arterial walls, and the presence of a vascular prosthesis, called a stent. The arterial wall is modeled as a two-layered structure, while the atheroma is modeled by the change in the elasticity coefficients in the thick structure layer. The stent is modeled by the change in the elasticity coefficients in the thin structure layer in places where the stent struts are located, forming a mesh-like pattern following the geometric distribution of struts in a particular stent. The two structural layers are coupled via the no-slip condition, and balance of forces, which models "glued" structures. In particular, the stent is glued to the atheroma region. Different coupling conditions may be used to capture different physical/physiological phenomena, including stent migration, or slip between the stent and atheroma, which has been associated with under-expanded stents.

Three examples were considered, each showing a new feature of the fluid-structure interaction model with composite structures, presented in this manuscript. The first example considers FSI between fluid flow and a two-layered cylindrical structure, showing the smoothing effects of the thin fluid-structure interface with mass. The second example considers FSI between fluid flow (blood flow) and a multi-layered structure (arterial wall) with a thick structure of varying stiffness and thickness (atheroma). The results show high intramural strains during cardiac cycle due to the presence of atheroma in the arterial wall. The third example considers FSI between fluid flow (blood) and a multi-layered structure (arterial wall), with a thick structure of varying stiffness and thickness to model atheroma, and a thin structure of varying stiffness to model a fully expanded vascular stent anchored to the arterial wall. Various novel pieces of information can be deduced from the simulations based

on investigating intramural displacement and strain distribution for both the radial and longitudinal displacements. Since the particular geometry of stent struts is well-captured, this model provides an indispensable tool to study the influence of different stent geometries on arterial intramural stress and strain distribution as well as flow patterns, all of which have been associated with an onset of a cascade of events leading to potential pathogeneses within the arterial wall. The model presented in this manuscript can be easily extended to more than two structural layers to capture a more realistic multi-layered structure of arterial walls.

6 Acknowledgements

All the authors would like to thank Professor Alfio Quarteroni for his support of this research and of D. Forti's visit to UH. Additionally, the research of D. Forti was supported by the Swiss National Foundation (SNF), project no. 140184. S. Deparis and D. Forti gratefully acknowledge the Swiss National Supercomputing Center (CSCS) for providing the CPU resources for the numerical simulations under project ID s475. The research of S. Canic and M. Bukac was supported by the US National Science Foundation under grant DMS-1318763, which also provided partial support for D. Forti's visit to the University of Houston. Additionally, the research of M. Bukac was supported by the US National Science Foundation under grant DMS-1619993. The research of S. Canic and A. Quaini was supported by the US National Science Foundation under grant DMS-1263572. Additionally, the research of A. Quaini was supported by the US National Science Foundation under grant DMS-1620384. Additionally, the research of S. Canic was supported by NSF DMS-1311709 and by the University of Houston Hugh Roy and Lillie Cranz Cullen Distinguished Professorship funds, which also provided additional travel support for D. Forti's visit to UH.

References

1. F. Alfonso, R.A. Byrne, F. Rivero, and A. Kastrati. Current treatment of in-stent restenosis (State-of-the-Art Paper). *Journal of the American College of Cardiology*, 63(24):2659–2673, 2014.
2. F.P.T. Baaijens. A fictitious domain/mortar element method for fluid-structure interaction. *Int. J. Numer. Meth. Fl.*, 35(7):743–761, 2001.
3. S. Badia, F. Nobile, and C. Vergara. Fluid-structure partitioned procedures based on Robin transmission conditions. *Journal of Computational Physics*, 227:7027–7051, 2008.
4. S. Badia, A. Quaini, and A. Quarteroni. Modular vs. non-modular preconditioners for fluid-structure systems with large added-mass effect. *Comput. Methods Appl. Mech. Engrg.*, 197(49-50):4216–4232, 2008.
5. D. Balzani, S. Deparis, S. Fausten, D. Forti, A. Heinlein, A. Klawonn, A. Quarteroni, O. Rheinbach, and J. Schröder. Numerical modeling of fluid-structure interaction in arteries with anisotropic polyconvex hyperelastic and anisotropic viscoelastic material models at finite strains. *Int J Numer Method Biomed Eng.* Published online, DOI:10.1002/cnm.2756.

6. A. T. Barker and X.-C. Cai. Scalable parallel methods for monolithic coupling in fluid-structure interaction with application to blood flow modeling. *Journal of Computational Physics*, 229(3):642 – 659, 2010.
7. Y. Bazilevs, V. M. Calo, Y. Zhang, and T. J. R. Hughes. Isogeometric fluid-structure interaction: Theory, algorithms and computations. *Comput. Mech.*, 43(1):3–37, 2008.
8. J. L. Berry, A. Santamarina, J. E. Moore Jr., S. Roychowdhury, and W. D. Routh. Experimental and computational flow evaluation of coronary stents. *Annal of Biomedical Engineering*, 28:386–398, 2000.
9. A. Bonito, R. Nochetto, and M. Pauletti. Dynamics of biomembranes: effect of the bulk fluid. *Mathematical modelling of natural phenomena*, 6(05):25–43, 2011.
10. M. Bukac, S. Canic, and B. Muha. A partitioned scheme for fluid-composite structure interaction problems. *Journal of Computational Physics*, 281:493 – 517, 2015.
11. S. Canic and E.H. Kim. Mathematical analysis of the quasilinear effects in a hyperbolic model of blood flow through compliant axisymmetric vessels. *Mathematical Methods in Applied Sciences*, 26(14):1161–1186, 2003.
12. P. Causin, J.F. Gerbeau, and F. Nobile. Added-mass effect in the design of partitioned algorithms for fluid-structure problems. *Comput. Methods Appl. Mech. Engrg.*, 194(42-44):4506–4527, 2005.
13. C. Colciago, S. Deparis, and A. Quarteroni. Comparisons between reduced order models and full 3D models for fluid–structure interaction problems in haemodynamics. *Journal of Computational and Applied Mathematics*, 265:120–138, 2014.
14. G.H. Cottet, E. Maitre, and T. Milcent. Eulerian formulation and level set models for incompressible fluid-structure interaction. *Esaim. Math. Model. Numer. Anal.*, 42:471–492, 2008.
15. P. Crosetto, S. Deparis, G. Fourestey, and A. Quarteroni. Parallel algorithms for fluid-structure interaction problems in haemodynamics. *SIAM Journal on Scientific Computing*, 33(4):1598–1622, 2010.
16. P. Crosetto, S. Deparis, G. Fourestey, and A. Quarteroni. Parallel algorithms for fluid-structure interaction problems in haemodynamics. *SIAM Journal on Scientific Computing*, 33(4):1598–1622, 2011.
17. S. Deparis, D. Forti, G Grandperrin, and A. Quarteroni. FaCSI: A block parallel preconditioner for fluidstructure interaction in hemodynamics. *Journal of Computational Physics*, 327:700 – 718, 2016.
18. W. G. Dettmer and D. Perić. A fully implicit computational strategy for strongly coupled fluid–solid interaction. *Archives of Computational Methods in Engineering*, 14(3):205–247, 2007.
19. J. Donea. *Arbitrary Lagrangian-Eulerian finite element methods, in: Computational methods for transient analysis*. North-Holland, Amsterdam, 1983.
20. C. Dumoulin and B. Cochelin. Mechanical behaviour modelling of balloon-expandable stents. *Journal of Biomechanics*, 33(11):1461–1470, 2000.
21. H. Fang, Z. Wang, Z. Lin, and M. Liu. Lattice Boltzmann method for simulating the viscous flow in large distensible blood vessels. *Phys. Rev. E.*, 65(5):051925–1–051925–12, 2002.
22. L.J. Fauci and R. Dillon. Biofluidmechanics of reproduction. In *Annual review of fluid mechanics. Vol. 38*, volume 38 of *Annu. Rev. Fluid Mech.*, pages 371–394. Annual Reviews, Palo Alto, CA, 2006.
23. Z.G. Feng and E.E. Michaelides. The immersed boundary-lattice Boltzmann method for solving fluid-particles interaction problems. *J. Comp. Phys.*, 195(2):602–628, 2004.
24. A. Figueroa, S. Baek, C. Taylor, and J. Humphrey. A computational framework for fluid–solid-growth modeling in cardiovascular simulations. *Computer methods in applied mechanics and engineering*, 198(45):3583–3602, 2009.
25. A. Figueroa, I.E. Vignon-Clementel, K. Jansen, T. Hughes, and C. Taylor. A coupled momentum method for modeling blood flow in three-dimensional deformable arteries. *Computer Methods in Applied Mechanics and Engineering*, 195(41-43):5685–5706, 2006.
26. A.L. Fogelson and R.D. Guy. Platelet-wall interactions in continuum models of platelet thrombosis: Formulation and numerical solution. *Math. Med. Biol.*, 21:293–334, 2004.
27. A.O. Frank, P.W. Walsh, and J. E. Moore Jr. Computational fluid dynamics and stent design. *Artificial Organs*, 26(7):614–621, 2002.

28. M. W. Gee, U. Küttler, and W. A. Wall. Truly monolithic algebraic multigrid for fluidstructure interaction. *International Journal for Numerical Methods in Engineering*, 85(8):987–1016, 2011.
29. B.E. Griffith. Immersed boundary model of aortic heart valve dynamics with physiological driving and loading conditions. *Int. J. Numer. Methods Biomed. Eng.*, 28(3):317–345, 2012.
30. B.E. Griffith. On the volume conservation of the immersed boundary method. *Commun. Comput. Phys.*, 12(2):401–432, 2012.
31. B.E. Griffith, R.D. Hornung, D.M McQueen, and C.S. Peskin. An adaptive, formally second order accurate version of the immersed boundary method. *J. Comput. Phys.*, 223(1):10–49, 2007.
32. B.E. Griffith, R. Luo, D.M. McQueen, and C.S. Peskin. Simulating the fluid dynamics of natural and prosthetic heart valves using the immersed boundary method. *Int. J. Appl. Mech.*, 1:137–177, 2009.
33. M. Heil. An efficient solver for the fully coupled solution of large-displacement fluid-structure interaction problems. *Computer Methods in Applied Mechanics and Engineering*, 193(1-2):1–23, 2004.
34. T. J. R. Hughes, W. K. Liu, and T. K. Zimmermann. Lagrangian-Eulerian finite element formulation for incompressible viscous flows. *Comput. Methods Appl. Mech. Engrg.*, 29(3):329–349, 1981.
35. T.J.R. Hughes, W.K. Liu, and T.K. Zimmermann. Lagrangian-Eulerian finite element formulation for incompressible viscous flows. *Computer Methods in Applied Mechanics and Engineering*, 29(3):329–349, 1981.
36. M. Krafczyk, M. Cerrolaza, M. Schulz, and E. Rank. Analysis of 3D transient blood flow passing through an artificial aortic valve by Lattice-Boltzmann methods. *J. Biomech.*, 31(5):453–462, 1998.
37. M. Krafczyk, J. Tölke, E. Rank, and M. Schulz. Two-dimensional simulation of fluid-structure interaction using lattice-Boltzmann methods. *Comput. Struct.*, 79(22-25):2031–2037, 2001.
38. K. W. Lau, A. Johan, U. Sigwart, and J. S. Hung. A stent is not just a stent: stent construction and design do matter in its clinical performance. *Singapore Medical Journal*, 45(7):305–312, 2004.
39. P. Le Tallec and J. Mouro. Fluid structure interaction with large structural displacements. *Computer Methods in Applied Mechanics and Engineering*, 190(24-25):3039–3067, 2001.
40. A. Leuprecht, K. Perktold, M. Prosi, T. Berk, W. Trubel, and H. Schima. Numerical study of hemodynamics and wall mechanics in distal end-to-side anastomoses of bypass grafts. *J. Biomech.*, 35(2):225–236, 2002.
41. S. Lim and C.S. Peskin. Simulations of the whirling instability by the immersed boundary method. *SIAM J. Sci. Comput.*, 25(6):2066–2083, 2004.
42. K.M. Marques, H.J. Spruijt, C. Boer, N. Westerhof, C.A. Visser, and F.C. Visser. The diastolic flow-pressure gradient relation in coronary stenoses in humans. *J. Am. Coll. Cardiol.*, 39:1630–1635, 2002.
43. D. R. McClean and N. Eigler. Stent design: Implications for restenosis. *MedReviews*, LLC, 2002.
44. F. Migliavacca, L. Petrini, M. Colombo, F. Auricchio, and R. Pietrabissa. Mechanical behavior of coronary stents investigated through the finite element method. *Jurnal of Biomechanics*, 35(6):803–811, 2002.
45. L.A. Miller and C.S. Peskin. A computational fluid dynamics of 'clap and fling' in the smallest insects. *J. Exp. Biol.*, 208(2):195–212, 2005.
46. J. E. Moore Jr. and J. L. Berry. Fluid and solid mechanical implications of vascular stenting. *Annals of Biomedical Engineering*, 30(4):498–508, 2002.
47. A. C. Morton, D. Crossman, and J. Gunn. The influence of physical stent parameters upon restenosis. *Pathologie Biologie*, 52(4):196–205, 2004.
48. B. Muha. A note on optimal regularity and regularizing effects of point mass coupling for a heat-wave system. *Journal of Mathematical Analysis and Applications*, 425(2):11341147.

49. B. Muha and S. Canic. Existence of a Weak Solution to a Nonlinear Fluid–Structure Interaction Problem Modeling the Flow of an Incompressible, Viscous Fluid in a Cylinder with Deformable Walls. *Archive for Rational Mechanics and Analysis*, 207(3):919–968, 2013.
50. B. Muha and S. Canic. "existence of a solution to a fluid-multi-layered-structure interaction problem. *Journal of Differential Equations*, 256:658–706, 2014.
51. F. Nobile. *Numerical approximation of fluid-structure interaction problems with application to haemodynamics*. PhD thesis, EPFL, Switzerland, 2001.
52. C. S. Peskin. Numerical analysis of blood flow in the heart. *J. of Comp. Phys*, 25:220–252, 1977.
53. C. S. Peskin. The Immersed Boundary method. *Acta Numer.*, 11:479–517, 2002.
54. A. Quaini and A Quarteroni. A semi-implicit approach for fluid-structure interaction based on an algebraic fractional step method. *Mathematical Models and Methods in Applied Sciences*, 17(6):957–985, 2007.
55. A. Quarteroni, M. Tuveri, and A. Veneziani. Computational vascular fluid dynamics: problems, models and methods. *Comput. Vis. Sci.*, 2(4):163–197, 2000.
56. J. Tambaca, S. Canic, M. Kosor, R.D. Fish, and D. Paniagua. Mechanical behavior of fully expanded commercially available endovascular coronary stents. *Tex. Heart Inst. J.*, 38:491–501, 2011.
57. T. E. Tezduyar, S. Sathe, and K. Stein. Solution techniques for the fully discretized equations in computation of fluidstructure interactions with the spacetime formulations. *Computer Methods in Applied Mechanics and Engineering*, 195(4143):5743 – 5753, 2006.
58. L. H. Timmins, M. R. Moreno, C. A. Meyer, J. C. Criscione, and J. E. Rachev, A. andMoore Jr. Stented artery biomechanics and device design optimization. *Med. Bio. Eng. Comput*, 45(5):505–513, 2007.
59. R. Van Loon, P.D. Anderson, J. De Hart, and F.P.T. Baaijens. A combined fictitious domain/adaptive meshing method for fluid-structure interaction in heart valves. *Int. J. Numer. Meth. Fl.*, 46(5):533–544, 2004.
60. Y. Wu and X.-C. Cai. A fully implicit domain decomposition based ALE framework for three-dimensional fluidstructure interaction with application in blood flow computation. *Journal of Computational Physics*, 258:524 – 537, 2014.
61. G. Zahnd, L. Boussel, A. Serusclat, and D. Vray. Intramural shear strain can highlight the presence of atherosclerosis: A clinical in vivo study. *Ultrasonics Symposium (IUS), 2011 IEEE International*, pages 1770 – 1773, 2011.